



Incorporation of spatially-resolved current density measurements with photoluminescence for advanced parameter imaging of solar cells

Mohammad Jobayer Hossain^a, Eric J. Schneller^b, Mengjie Li^b, Kristopher O. Davis^{a,b,*}

^a CREOL, The College of Optics and Photonics, University of Central Florida, Orlando, FL 32816, USA

^b Department of Materials Science and Engineering, University of Central Florida, Orlando, FL 32816, USA

ABSTRACT

The spatial distribution of device performance parameters of solar cells provides important insight into their operation, including the type and magnitude of conversion losses and potential areas of improvement. In most of the procedures used to create these parameter images, a uniform (i.e., global) short-circuit current density (J_{SC}) is usually assumed. However, J_{SC} is known to vary over the surface of a solar cell, especially in polycrystalline absorber materials like multicrystalline silicon. In this work, a high speed quantum efficiency measurement rastered over the surface of a solar cell is used to obtain images of J_{SC} . These J_{SC} images are then used to calculate images of series resistance, dark saturation current density, fill factor, and conversion efficiency. Comparisons are made between the images created with a global J_{SC} and with the spatially-resolved J_{SC} . Negligible variation is observed in the series resistance and dark saturation current density images, but a drastic change is observed in the efficiency images between these two methods.

1. Introduction

Traditional solar cell characterization techniques like illuminated current-voltage (I – V , J – V) and Suns- V_{OC} provide a single value (i.e., global) for the performance parameters of a solar cell, like the conversion efficiency (η), short-circuit current density (J_{SC}), open-circuit voltage (V_{OC}), fill factor (FF), dark saturation current density (J_0), and series resistance (R_s). However, solar cells are large area devices that often have significant variation in these parameters over the surface of the entire device. Photoluminescence (PL) imaging is a method commonly used by the photovoltaics (PV) industry and R&D community to determine the spatial distribution of these parameters. The speed and relative simplicity of the measurement make it applicable as both an off-line and in-line metrology technique.

There have been numerous efforts to obtain spatial distributions of the performance parameters from both PL and electroluminescence (EL) signals. Fuyuki et al. developed a way of determining the spatial distribution of minority carrier diffusion length from EL [1]. PL imaging with an electrical bias have been used to obtain images of R_s [2,3]. Glatthaar et al. mathematically derived the spatial voltage distribution from the luminescence images of a silicon solar cell and two different models namely terminally connected diodes and interconnected diodes for determination of spatial maps of the physical parameters [4]. PL imaging has also been used to obtain images of efficiency [5–7] and the recombination occurring in the perimeter of the cell [8]. In all of the methods above, a global value of J_{SC} is assumed. It has been

demonstrated that J_{SC} is not actually uniform, but instead varies spatially across the cell. The impact of this assumption on the resulting parameter images is not clear. Several authors have suggested that it may result in substantial inaccuracies [6,7,9,10].

In this work, the impact of using a global J_{SC} value is investigated. We explore how this assumption influences the images obtained for efficiency, FF , J_0 , and R_s . The J_{SC} images used in this work are obtained using a high-speed external quantum efficiency (EQE) and reflectance measurement system capable of rastering over the entire surface of solar cells, a technique introduced previously [11,12]. Images of efficiency, FF , J_0 , and R_s are created using both the global J_{SC} and the spatially-resolved J_{SC} . Additionally, two different methods of determining the efficiency and FF are also compared: one relies on the PL image when the terminal voltage is set to the max-power voltage; the other relies on the generation of a J – V curve using the various parameters obtained and the Shockley diode equation. Finally, the approach presented here can be used to diagnose the root cause of defective areas within a solar cell by further analyzing the QE and reflectance images and decoupling losses based on position (i.e., front or rear side of the device) and mechanism (e.g., reflectance, parasitic absorption, recombination).

2. Methodology

The methodology presented in this work relies on the spatially-resolved EQE data as a direct measurement of the local J_{SC} , which is

* Corresponding author.

E-mail address: kristopher.davis@ucf.edu (K.O. Davis).

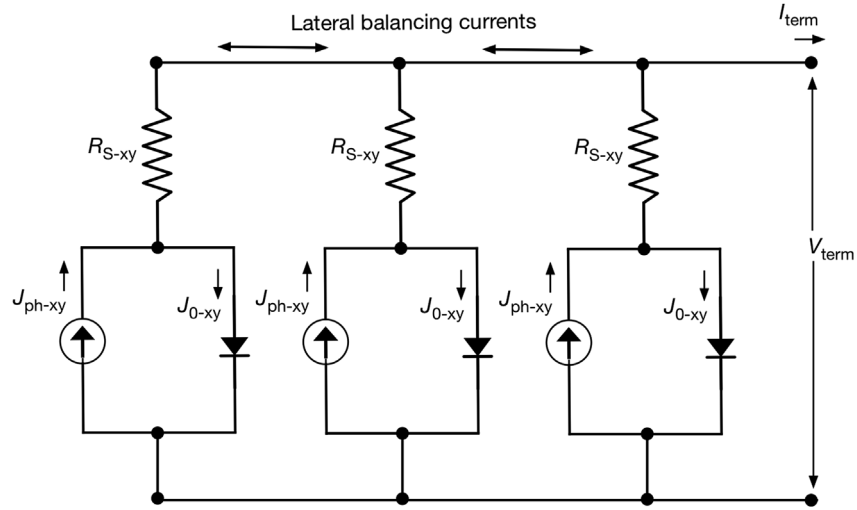


Fig. 1. Illustration of the terminal connected diode model from Ref. [17].

assumed to be equal to the local photogenerated current density (J_{ph}). PL images are then captured under various external bias and illumination conditions to generate images of local voltage. From there, images of cell performance parameters are obtained using the methods outlined in this section.

2.1. Local photogenerated current

The local photogenerated current J_{SC-xy} is obtained at each point on the solar cell using the following equation [12,13],

$$J_{SC} = e \int_{365nm}^{1200nm} \Phi_{inc}(\lambda) EQE(\lambda) d\lambda \quad (1)$$

Here e , EQE and Φ_{inc} are the charge of an electron, external quantum efficiency and incident photon flux respectively. An AM1.5G solar spectrum from 365 nm to 1200 nm was considered for this calculation.

2.2. Local voltage

The well-known correlation between luminescence intensity and local voltage of a semiconductor substrate or solar cell results in the following expression relating the luminescence intensity Φ_{xy} at a position (x,y) to the local voltage at that same position [2,14]:

$$\Phi_{xy} = C_{xy} \exp\left(\frac{V_{xy}}{V_T}\right) + \Phi_{offset} \quad (2)$$

Here, V_{xy} and V_T are the local junction voltage and thermal voltage respectively. C_{xy} is a calibration constant independent of both the electrical bias and the illumination conditions. The offset part of luminescence intensity Φ_{offset} emerges because of the diffusion limited (i.e., voltage-independent) carrier recombination [2,15,16]. It is proportional to the illumination intensity I_L and can be expressed as

$$\Phi_{offset} = B_{xy} \cdot I_L \quad (3)$$

Here B_{xy} refers to the background luminescence signal. According to Glatthar's approximation [4], for a PL image taken at the same illumination condition I_L with the cell operating in the short-circuit condition, the resulting PL intensity becomes equal to the offset PL intensity, Φ_{offset} [17]. The background B_{xy} is calculated from this short-circuit PL image Φ_{offset} . Substituting Φ_{xy-SC} for Φ_{offset} and I_{L-SC} for I_L we can write,

$$B_{xy} = \frac{\Phi_{xy-SC}}{I_{L-SC}} \quad (4)$$

The calibration constant C_{xy} is determined from an open-circuit PL image Φ_{low} , taken with a sufficiently low illumination I_{low} ,

$$C_{xy} = [\Phi_{xy-low} - B_{xy} \cdot I_{low}] \cdot \exp\left(-\frac{V_{OC-low}}{V_T}\right) \quad (5)$$

Here, V_{OC-low} is the measured open-circuit voltage at the low illumination intensity I_{low} . The key assumption is that, at a sufficiently low illumination intensity, the lateral gradient of open-circuit voltage is negligible. The intensity regime considered to be 'sufficiently low' was investigated by Hoffler [17]. They observed that for 0.19 sun illumination, the maximum voltage difference over a multicrystalline silicon cell was only 5 mV, concluding that 0.19 sun was sufficient for the calibration purpose. For this work, a conservative illumination intensity of 0.1 sun was used to capture the open-circuit PL image used in the calculation of C_{xy} . With C_{xy} and B_{xy} , the voltage distribution V_{xy} can be determined for any arbitrary PL image Φ_{xy} using the following relation,

$$V_{xy} = V_T \cdot \ln\left(\frac{\Phi_{xy} - B_{xy} \cdot I_L}{C_{xy}}\right) \quad (6)$$

2.3. Local series resistance and dark saturation current density

Images for R_{S-xy} and J_{0-xy} can be calculated using the terminal connected diode model shown in Fig. 1 [4,17]. In this model, a solar cell can be considered as a combination of parallel diodes which are connected to a common terminal through their individual series resistances. The figure comprises of three units (three parallel diodes) each having a distinct J_{ph-xy} , R_{S-xy} , and J_{0-xy} . An infinite shunt resistance is typically assumed for analysis purposes. With V_{term} and n as the terminal voltage and the ideality factor of the diode, respectively, then this model results in the following equation,

$$V_{term} - V_{xy} = R_{S-xy} \left[J_{0-xy} \exp\left(\frac{V_{xy}}{nV_T}\right) - J_{ph-xy} \right] \quad (7)$$

For the ideality factor, a global n can be assumed as an ideal diode ($n = 1$) [4,17] or a variable n can be used [6]. A spatially-resolved ideality factor can also be used [7,18]. In this work, we use a global n for simplicity and compare the cases where $n = 1$ and the more realistic case where n is not equal to 1. In previous works to date, a global J_{SC} was assumed for quantitative PL techniques. As mentioned previously, in this work a point-by-point J_{SC-xy} measurement is obtained, which we use as J_{ph-xy} in this analysis (i.e., $J_{SC-xy} = J_{ph-xy}$).

R_{S-xy} and J_{0-xy} are the two remaining unknowns in equation (7). Therefore two additional measurements with different terminal

voltages, but the same illumination condition is required.

2.4. Local efficiency using PL at $V = V_{MPP}$

To calculate the efficiency image of the cell, we need V_{MPP-xy} and J_{MPP-xy} distribution over the cell. In this work, two methods of obtaining these distributions were investigated. The first method relies on obtaining V_{MPP-xy} and J_{MPP-xy} from an additional PL image. To achieve this, an additional biased PL measurement was done at global V_{MPP} value of the cell at 1 sun condition (which comes from the illuminated I – V measurement). Plugging it into equation (6) provides a V_{MPP-xy} distribution of the cell. Then J_{MPP-xy} is obtained from the single diode model J – V curve [6,19].

$$J_{MPP-xy} = J_{SC-xy} - J_{0-xy} \left[e^{\frac{V_{MPP-xy}}{n_{xy} V_T}} - 1 \right] \quad (8)$$

The efficiency image can be calculated using,

$$Eff_{xy} = \frac{P_{out-xy}}{P_{in}} = \frac{V_{MPP-xy} \cdot J_{MPP-xy}}{1000 W m^{-2}} \quad (9)$$

Here $P_{in} = 1000 W m^{-2}$ is the input power density used in our experiment as the standard test condition. Noticeably the spatial distribution of the J_{SC} (i.e. J_{SC-xy}) is used in equation (9) as opposed to the previous works that used a uniform J_{SC} [19].

2.5. Local efficiency and fill factor using J – V curve fit

To provide additional insights into the impact of a spatially resolved current density, a method using locally generated J – V curves to calculate efficiency was also explored. The method is similar to the approach introduced by Breitenstein [20,21]. In their approach, dark lock-in thermography is used to generate key parameter maps including J_{01} and J_{02} and a 2-diode model is used to model each individual pixel. In this work, PL imaging is used to generate parameter maps for R_s and J_0 and EQE data is used to generate J_{SC} maps. The key difference here is the use of a single diode equation where the ideality factor can be adjusted. Since we have the local value of J_{SC} , J_0 and R_s , we can plug these into the diode equation,

$$J_{xy} = J_{SC-xy} - J_{0-xy} \left[\exp\left(\frac{V_{xy} + R_{s-xy} \cdot J_{xy}}{n V_T}\right) - 1 \right] \quad (11)$$

V_{MPP-xy} and J_{MPP-xy} are obtained by finding the maximum power point of the J – V curve in equation (11). Then the local efficiency images can be calculated using equation (9).

The FF_{xy} image can be obtained from V_{MPP-xy} and J_{MPP-xy} using,

$$FF_{xy} = \frac{V_{MPP-xy} \cdot J_{MPP-xy}}{V_{OC-xy} \cdot J_{SC-xy}} \quad (12)$$

Here V_{OC-xy} is the spatially resolved open circuit voltage distribution over the cell.

To compare the two methods of efficiency calculation, the first method requires an I – V measurement and PL measurement at ‘global MPP’, whereas the second method requires two additional biased PL images from which it determines the voltage and current density images at ‘local MPP’, other variables being the same. The second method requires more computational power as it requires an independent determination of the J – V curve for each pixel in the image.

3. Experimental details

An industrial multicrystalline Si Al-BSF solar cell was used in this work, featuring a silicon nitride (SiN_x) antireflection coating, isotropic texturing, screen-printed contacts, and an overall area of $243 cm^2$. A multicrystalline cell was chosen due to the larger spatial variation in J_{SC} and J_0 compared to monocrystalline solar cells. A Tau Science FlashQE

system was used to measure the external quantum efficiency (EQE) and reflectance (R) over the surface of the cell. This system uses individually controlled LEDs featuring 41 distinct wavelengths (λ) between 365 nm and 1280 nm. These LEDs act as the spectrally-resolved light source and have an illuminated spot size of approximately 3 mm. The system has electronics to measure the current at each wavelength for $EQE(\lambda)$ and an integrating sphere with photodetectors to measure $R(\lambda)$. A full-spectrum $EQE(\lambda)$ and $R(\lambda)$ measurement is performed simultaneously in 1 s. This measurement system was programmed to raster over the entire surface of the solar cell to create a 97×97 image of $EQE(\lambda)$ and $R(\lambda)$ [12,22]. The resulting $97 \times 97 J_{SC-xy}$ image was then converted into a 960×960 image using a linear interpolation. This interpolation was performed to achieve the same number of matrix elements in both the J_{SC-xy} images and the PL images. The mean J_{SC} (i.e., averaged over the entire surface of the cell) of the original 97×97 image and the interpolated 960×960 image are equal ($J_{SC} = 32.2 mA/cm^2$). Performing interpolation on a low-resolution image is not unusual; the linear interpolation was used previously on current density images using the LBIC method [10]. Once the J_{SC-xy} image was obtained, it was then used to calculate images of R_s , J_0 , FF , and efficiency.

Illuminated I – V measurements were performed with a BT Imaging LIS-R1 system with an 808 nm laser as the light source. First, to determine the one sun condition, global J_{SC} measurements were performed on the cell and the photon flux was varied until the global J_{SC} measured matches the spatially averaged J_{SC} obtained from the QE measurement. For the cell used in this study, a photon flux of $3.06 \times 10^{17} cm^{-2}s^{-1}$ and $3.06 \times 10^{16} cm^{-2}s^{-1}$ were considered as the 1 sun and 0.1 suns respectively. The global cell parameters were obtained for the cell using the 1 sun illuminated I – V curve from the LIS-R1 system (Table 1). The cell showed an overall efficiency of 15.40%, with $J_{SC} = 32.2 mA/cm^2$ and $V_{OC} = 0.612 V$. The global value for R_s was obtained using Suns- V_{OC} and illuminated IV curves following the method in Ref. [23]. The global J_0 and n were obtained via curve fitting with the software tool described in Ref. [24] which are $3.39 \times 10^{-10} A/cm^2$ and 1.3 respectively.

The LIS-R1 system was also used for the PL imaging. It features an 808 nm laser, 920 nm long-pass filter, and 1-megapixel silicon CCD camera. The LIS-R1 system also features a test chuck and power supply to electrically bias solar cells during the imaging process. Two biased PL images were taken at 1 sun for the calculation of R_{s-xy} and J_{0-xy} . A PL image at 0.1 suns with the device at open-circuit ($J = 0$) was taken and a 1 sun image with the device at short-circuit ($V = 0$) were taken for the calculation of the background (equation (4)) and the 1 sun V_{OC-xy} image. An additional biased PL image was taken at 1 sun with the device held at the MPP ($V = V_{MPP}$) to obtain efficiency images for one of the methods explored.

4. Results and discussion

4.1. Current and voltage images

The $97 \times 97 J_{SC}$ image obtained from the spatially-resolved EQE data and equation (1) is shown in Fig. 2(a). To be able to use both the

Table 1

Global values of the cell parameters calculated from illuminated I – V and Suns- V_{OC} measurement.

Parameter	Value
Efficiency	0.15
J_{SC}	32.2 mA/cm ²
V_{OC}	0.61 V
FF	0.78
R_s	0.2 Ω -cm ²
Ideality factor	1.3
J_0	$3.39 \times 10^{-10} A/cm^2$

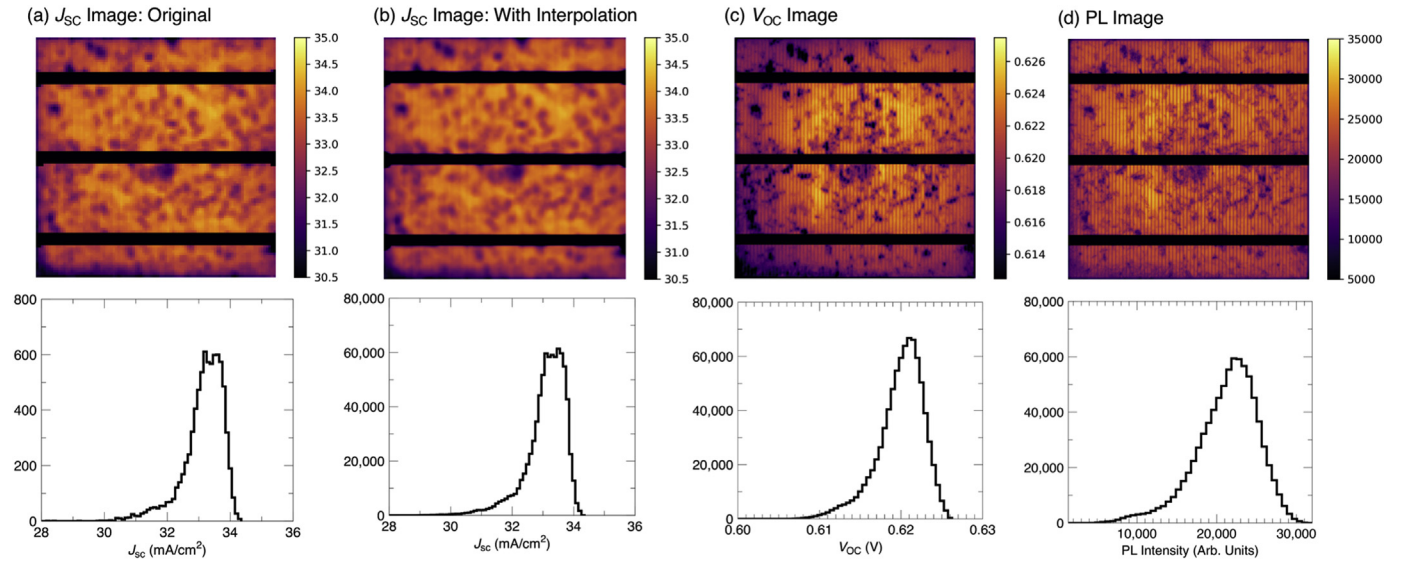


Fig. 2. Images of J_{SC} , V_{OC} , and the uncalibrated PL signal and their histograms: (a) Original J_{SC} image of size 97×97 pixels; (b) interpolated J_{SC} images 960×960 pixels; (c) V_{OC} image; and (d) uncalibrated PL image.

J_{SC-xy} and V_{OC-xy} images together in the same equation for further analysis, the matrix size has to be the same for both parameters. To increase the matrix size of the J_{SC-xy} image, a spatial linear interpolation was used, as shown in Fig. 2(b). Both the original and interpolated J_{SC-xy} images and their histograms appear very similar and have equivalent spatial averages (32.2 mA/cm^2). This spatial average includes the busbar regions of the cells and is equal to the global J_{SC} shown in Table 1. Since little information can be gained from the busbar region, this region is excluded for the analysis presented in this work. The global current density excluding the busbar regions (from global I - V curve) is 33.1 mA/cm^2 , which is close to the mode of the J_{SC-xy} histogram. Noticeably, the shape of the histogram is not a symmetrical Gaussian curve but is skewed, featuring a tail on the lower end of the histogram arising from the presence of the J_{SC} loss mechanisms.

Fig. 2(c) shows the V_{OC} image and histogram of the cell calculated using the necessary PL images and equation (6). The uncalibrated PL image taken at one sun and at open-circuit is shown in Fig. 2(d). Looking at all of the images in Fig. 2, it's clear that the presence of the grain boundaries and dislocations affects the PL signal, the local voltage, and the local current. The patterns are noticeably similar for the J_{SC} and V_{OC} images, with dark regions showing up in both. This is due to the known reciprocity between luminescence and quantum efficiency of a solar cell [25]. Locations with strong PL emission also have strong QE response (i.e. higher local current and voltage). The spatial average of V_{OC} distribution is 0.62 V , which lies as the mode of the V_{OC} histogram, similar to J_{SC} .

4.2. Series resistance and saturation current density images

Series resistance (R_S) and dark saturation current density (J_0) are two important parameters of a solar cell which influence the shape of the I - V curve. The terminal connected diode model in equation (7) allows the determination of R_S and J_0 maps from two biased PL images. Fig. 3 presents four images of R_S and four images of J_0 for the same cell, where the images were created using different inputs for J_{SC} (i.e., global J_{SC} versus J_{SC-xy}) and for the global ideality factor (ideal diode case, $n = 1$ versus actual case, $n = 1.3$). Unlike the V_{OC} and J_{SC} images, the R_S and J_0 images are very different from each other. The dislocations and high recombination crystal grains seen in the J_0 images are not evident in R_S images, as expected. The vertically aligned rectangular features with high resistance seen in the R_S images, denoted by dashed green rectangles in the top left image of Fig. 3(a), are the well known

sign of broken gridlines at the front of the cell [2].

Comparing the histograms for R_S , the increase in the ideality factor results in a slightly higher mode of about $0.1 \Omega\text{-cm}^2$ for R_S and minor broadening of the distribution. The shape of the R_S distribution is rather symmetrical, lacking the skew observed in the distributions of J_{SC} and V_{OC} (Fig. 2). The difference between the assumption of a global J_{SC} and spatially-resolved J_{SC-xy} makes virtually no difference for both ideality factors. This suggests that the use of a global J_{SC} is a safe assumption when creating R_S images.

The J_0 images in Fig. 3(b) illustrate the distribution of recombination losses across the solar cell. Crystallographic defects like dislocation clusters and recombination active grain boundaries, as well as regions featuring higher concentrations of deleterious impurities (e.g., Fe) are the most common causes of the local regions with high J_0 . The shape of the J_0 distribution shown in the histograms is skewed like the V_{OC} and J_{SC} distribution from Fig. 2. In the case of J_0 though, the tail is on the higher end of the distribution. This makes sense as the regions with a high J_0 would be expected to have a low V_{OC} and low J_{SC} . J_0 is on the order of 10^{-12} A/cm^2 for the ideal diode assumption of $n = 1$, and as expected, it is much higher for the $n = 1.3$ case (10^{-10} A/cm^2). There is no perceivable change in the J_0 images after incorporation of the spatially-resolved J_{SC-xy} rather than a global J_{SC} . As in the case of R_S , this suggests global J_{SC} is a safe assumption for calculating the local J_0 . In all four of the J_0 images, there is no sign of the R_S defects like the vertical rectangles caused by broken gridlines. This indicates that all of the assumptions here successfully decouple the resistive losses from the recombination losses.

4.3. Efficiency and fill factor images

Fig. 4 presents the efficiency images for both methods discussed previously. The colorbars for all images in this figure are scaled independently using the 1st percentile and 99th percentile as the minimum and maximum, respectively, excluding busbars. This is done to aid in the visual comparison. The incorporation of the spatial current density has a significant impact on the derived efficiency images. There is an increase in the contrast between the good and bad regions of the device. The histograms clearly describe this impact, as the distribution of efficiency has both shifted and widened with the incorporation of J_{SC-xy} . When an ideal diode is considered (i.e., $n = 1$), the mean increased from 16.8% to 17.5% and when the actual global ideality factor of 1.3 is used, the mean increased from 16.4% to 17.1%. The efficiency images

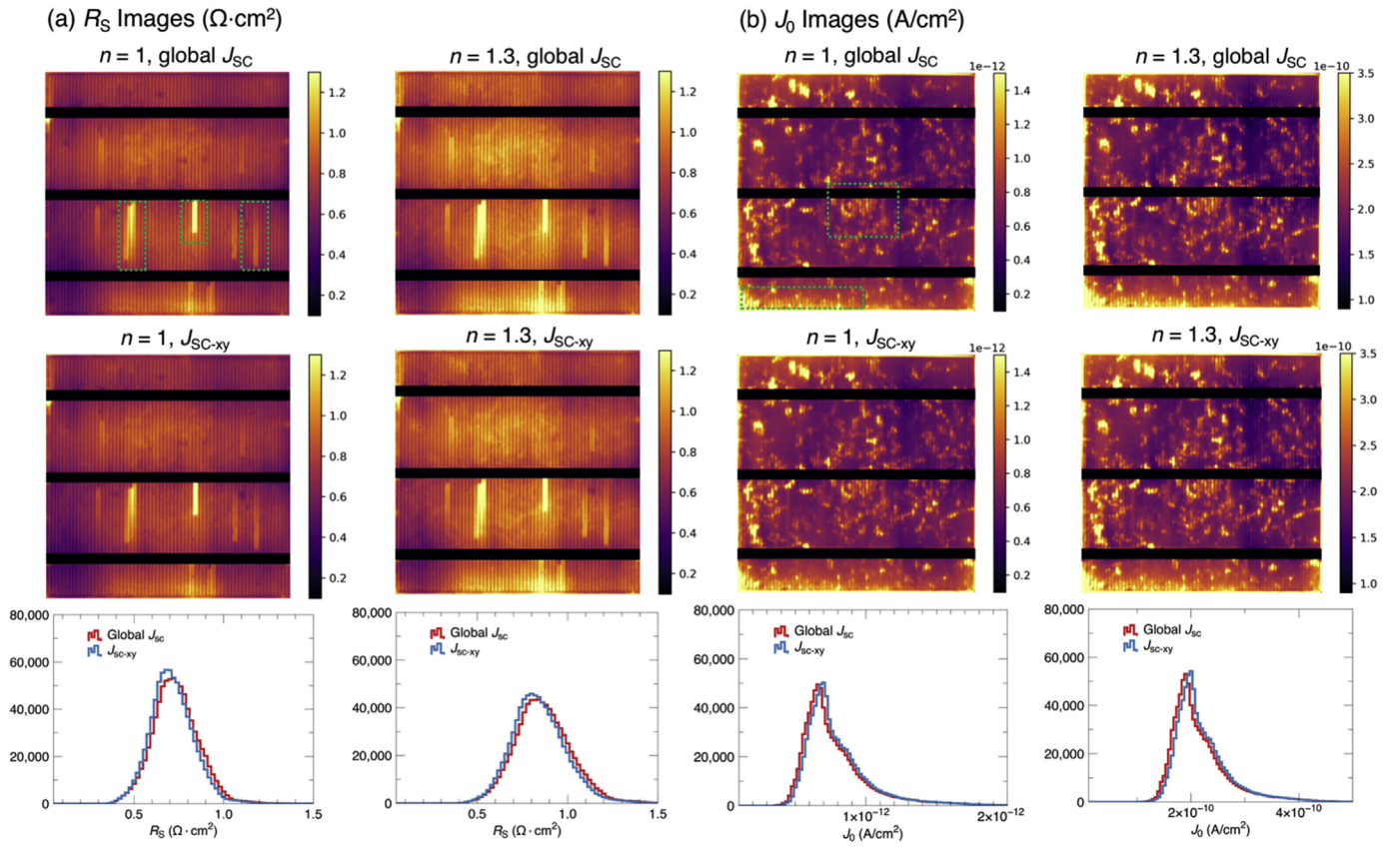


Fig. 3. (a) Series resistance images and histograms. (b) Dark saturation current density images and histograms.

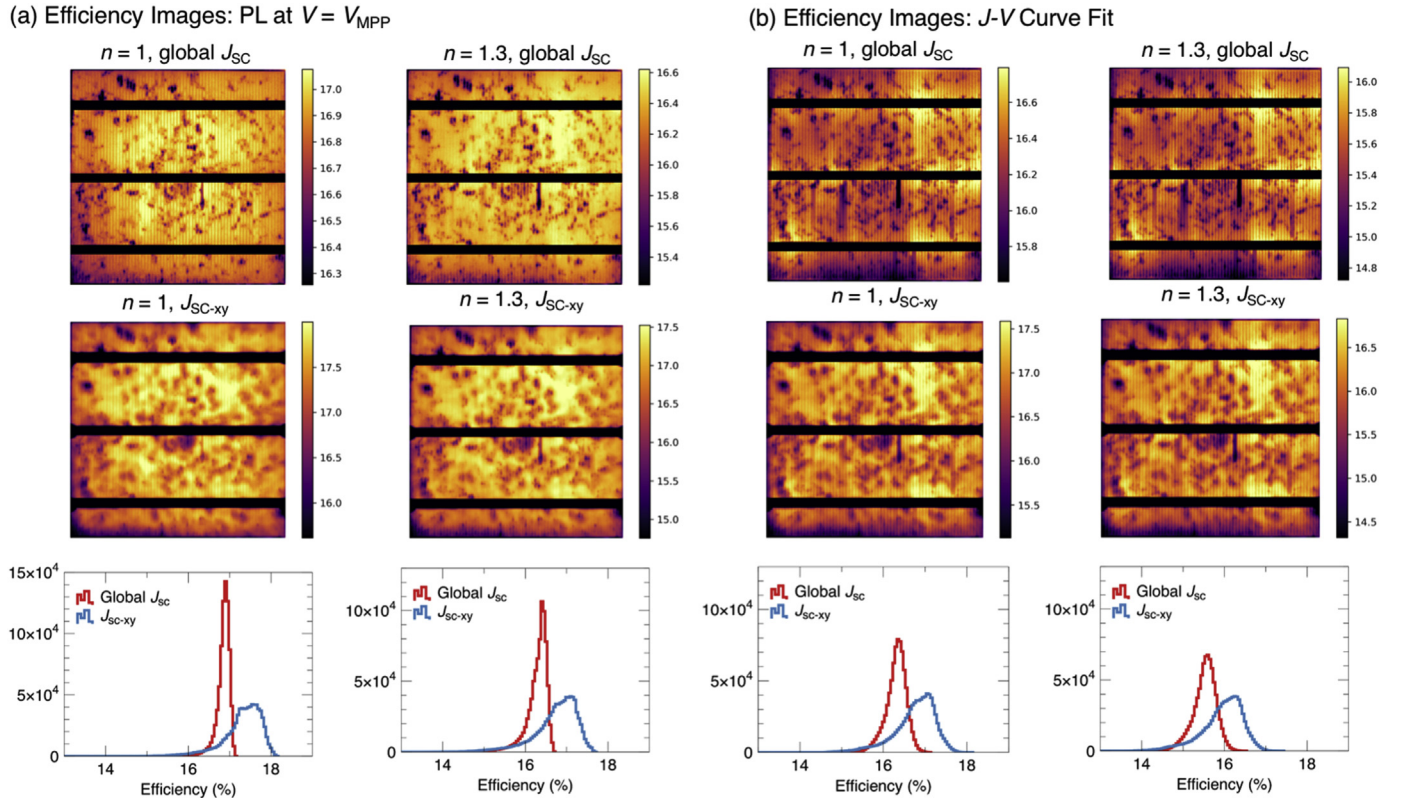


Fig. 4. Efficiency images and histograms using: (a) the PL image at a bias voltage of $V = V_{MPP}$; and (b) the J-V curve fitting method.

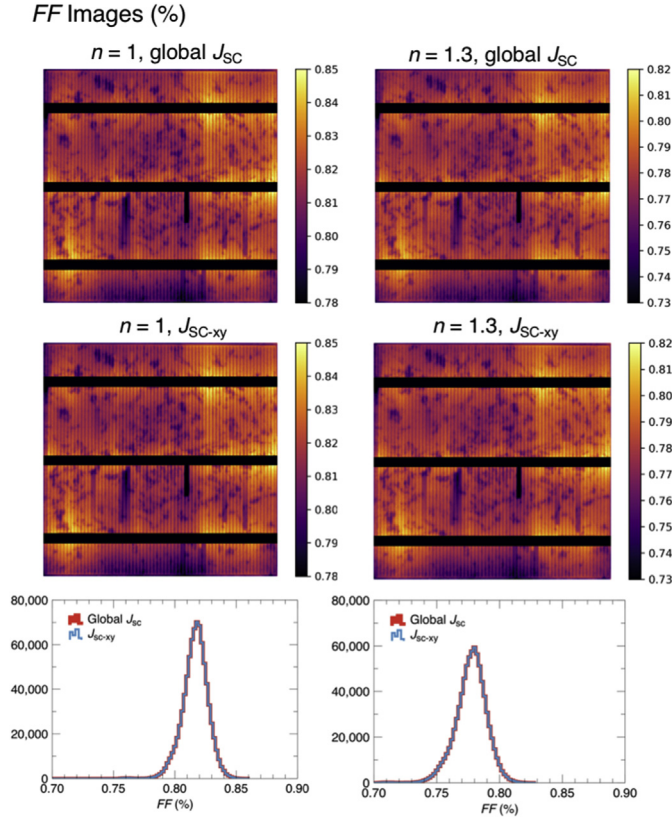


Fig. 5. Fill factor images and histograms.

are largely influenced by recombination losses including the sites associated with dislocations and grain boundaries. It is worth mentioning here that we did not separate the edge recombination from the total recombination in the device for simplicity; edge recombination can lead to reduced efficiency value of a cell [8]. Series resistance related defects appear to have only a minor influence on the local efficiency, although these regions are more pronounced in the J - V curve fit method. For both methods, the resulting efficiency images including J_{SC-xy} have remarkably similar distributions.

Although it is not directly related to optoelectronic properties, the fill factor is useful in performance evaluation of a solar cell. It dictates the shape of the I - V curve. A spatial map of fill factor could account for the relative difference of performance over the surface of a cell. The fill factor images in Fig. 5 are affected by both the series resistance and the dark saturation current density. Increasing the ideality factor from 1 to 1.3 lead to a decrease in the mean fill factor from 0.82 to 0.78. For both cases, incorporation of spatial current density does not change the fill factor at all. Fill factor is a ratio between the maximum power of the I - V curve and the maximum power attainable if there was no loss present.

4.4. Loss analysis using quantum efficiency

The images of EQE and R used to create the J_{SC-xy} input parameter in this work can also be used for loss analysis of the solar cell. This is particularly useful when trying to attribute optical and recombination losses to a particular layer or interface within the device. The details of this approach were described in prior work [12,26], but here we provide a brief description for the sake of information. The internal quantum efficiency (IQE) at a point over the cell can be calculated from the measured value of EQE and R at that point,

$$IQE(\lambda) = \frac{EQE(\lambda)}{1 - R - f_{eff}} \quad (13)$$

Here f_{eff} is the effective optical shaded fraction within the measurement light-spot, occurring due to the presence of the gridlines. Now according to the model proposed by Fischer et al., IQE can be expressed in terms of the effective diffusion length (L_{eff}), absorption length of silicon (L_a) and an scaling factor (k) as following,

$$IQE(\lambda) = \frac{1}{k} \exp\left(-\frac{W_d}{L_a(\lambda)}\right) \frac{1}{1 + \frac{L_a(\lambda)}{L_{eff}}} \quad (14)$$

Here W_d is the thickness of a hypothetical dead layer which accounts for the parts of the emitter which do not contribute to the photogenerated current because of recombination occurring. L_a is used from the literature and IQE from equation (13). Running a simple iterative process starting with the reasonable guess for the rest of the parameters provides the value of k , L_{eff} and W_d . Here, the slope and intercept of the $\ln\left(IQE \cdot \left(1 + \frac{L_a}{L_{eff}}\right)\right)$ vs. $\frac{1}{L_a}$ plot at any wavelength provides the values for W_d and k respectively at that wavelength. These values are then used for plotting $\frac{1}{IQE} \exp\left(\frac{W_d}{L_a}\right)$ vs. L_a graph which then provides the values for L_{eff} and k . This iterative process continues until it converges to the actual values of k , L_{eff} and W_d .

Once the L_{eff} and W_d and values become available, they can be used for calculating the losses in emitter. The total loss in emitter can be divided into two discrete wavelength regimes: (I) 365 nm - 500 nm, where the dead layer approximation is inadequate and (II) 500 nm - 1280 nm, where the dead layer approximation is reasonable. With this, the IQE loss in emitter can be expressed as,

$$IQE_{loss,emi,I} = 1 - IQE(\lambda) \cdot \left(1 - \frac{L_a(\lambda)}{L_{eff}}\right) \quad (15a)$$

$$IQE_{loss,emi,II} = 1 - \exp\left(-\frac{W_d}{L_a(\lambda)}\right) \quad (15b)$$

Now the total current loss in emitter (J_{loss-e}) can be calculated from the these IQE loss values. The rest of the parasitic loss is then attributed to the loss in the base (J_{loss-b}).

Fig. 6 shows results of such analysis including maps of the L_{eff} , current loss in the emitter (J_{loss-e}) and current loss in the base (J_{loss-b}) and compares this with what is seen in the PL image. Regions associated with a high density of dislocations are highlighted in green and are associated with lower effective diffusion lengths and higher current loss in the base of the device. The same regions also showed high magnitude in the J_0 image (Fig. 3) and low magnitude in the J_{SC} (Fig. 2(a)) and V_{OC} (Fig. 2(c)) images. The current loss in the base is significantly larger than the current loss in the emitter. Although the impact is minor, the spatial variation of the dopant concentration in the emitter, with a higher dopant concentration near the edges of the device, can be identified in Fig. 6(b). This pattern is not present in any of the parameter maps derived from PL images alone. The combination of both spatially resolved PL and QE provides a complete picture of where the losses are occurring within the device and the impact they have on overall performance.

5. Conclusion

In this work, a method of using the local photogenerated current as an input to create images of solar cell parameters (e.g., efficiency) is presented. Various methods of extracting cell parameters images using photoluminescence were carried out on the same multicrystalline silicon Al-BSF solar cell with an emphasis on any changes that occur when assuming a uniform global J_{SC} across the entire cell versus a local J_{SC-xy} obtained using spatially-resolved quantum efficiency measurements. The application of a local J_{SC-xy} had a negligible influence on the extraction of R_s , J_0 , and fill factor, indicating the use of a global J_{SC} is likely a valid assumption for these parameters. In stark contrast, the use

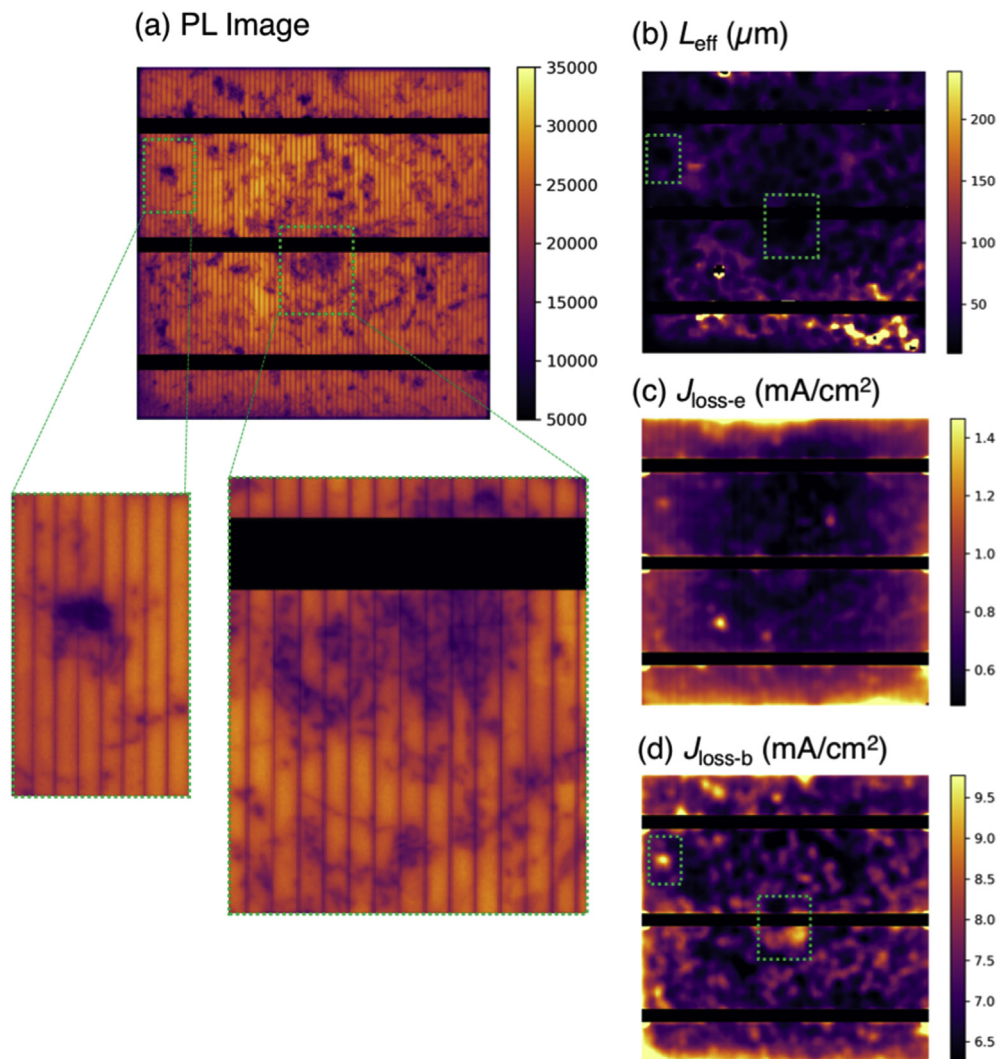


Fig. 6. The results of the current loss analysis: (a) PL image; (b) effective diffusion length; (c) emitter loss (d) and bulk and rear loss due to recombination and parasitic optical absorption.

of a local J_{SC-xy} had a large influence on the extraction of local cell efficiency, increasing the mode of the local efficiency histogram and broadening the distribution. Additionally, this method has the benefit of using the spatially-resolved quantum efficiency and reflectance data for loss analysis when evaluating areas with particular poor performance (e.g., high J_0 , low efficiency). This can be used to identify the root cause of manufacturing defects and to evaluate how spatial variance in parameters like the effective diffusion length, current loss in the emitter, current loss in the base, front surface reflectance losses, and escape reflectance.

Acknowledgements

This work is supported by the U.S. Department of Energy's Solar Energy Technologies Office under grant numbers DE-EE-0008155.

Appendix A. Supplementary data

Supplementary data to this article can be found online at <https://doi.org/10.1016/j.solmat.2019.04.012>.

References

- [1] T. Fuyuki, H. Kondo, Y. Kaji, T. Yamazaki, Y. Takahashi, Y. Uraoka, One shot

- mapping of minority carrier diffusion length in polycrystalline silicon solar cells using electroluminescence, Conference Record of the Thirty-First IEEE Photovoltaic Specialists Conference, IEEE, 2005, <https://doi.org/10.1109/pvsc.2005.1488390>.
- [2] T. Trupke, E. Pink, R.A. Bardos, M.D. Abbott, Spatially resolved series resistance of silicon solar cells obtained from luminescence imaging, *Appl. Phys. Lett.* 90 (9) (2007) 093506 <https://doi.org/10.1063/1.2709630>.
- [3] H. Kampwerth, T. Trupke, J.W. Weber, Y. Augarten, Advanced luminescence based effective series resistance imaging of silicon solar cells, *Appl. Phys. Lett.* 93 (20) (2008) 202102 <https://doi.org/10.1063/1.2982588>.
- [4] M. Glatthaar, J. Haunschild, R. Zeidler, M. Demant, J. Greulich, B. Michl, W. Warta, S. Rein, R. Preu, Evaluating luminescence based voltage images of silicon solar cells, *J. Appl. Phys.* 108 (1) (2010) 014501 <https://doi.org/10.1063/1.3443438>.
- [5] Otwin Breitenstein, Chao Shen, Henner Kampwerth, A. Martin, Green, Comparison of DLIT- and PL-based local solar cell efficiency analysis, *Energy Procedia* 38 (2013) 2–12 <https://doi.org/10.1016/j.egypro.2013.07.243>.
- [6] Chao Shen, A. Martin, Green Otwin Breitenstein, Trupke Thorsten, Zhang Muye, Kampwerth Henner, Improved local efficiency imaging via photoluminescence for silicon solar cells, *Sol. Energy Mater. Sol. Cells* 123 (April) (2014) 41–46 <https://doi.org/10.1016/j.solmat.2014.01.003>.
- [7] Kortan Ögütman, Kristopher O. Davis, Eric Schneller, Vijay Yelundur, Winston V. Schoenfeld, Integration of spatially resolved ideality factor into local cell efficiency analysis with photoluminescence, *Sol. Energy* 158 (December) (2017) 869–874 <https://doi.org/10.1016/j.solener.2017.10.006>.
- [8] Kean Chern Fong, Milan Padilla, Andreas Fell, Evan Franklin, Keith R. McIntosh, Teng Choon Kho, Andrew W. Blakers, Yona Nebel-Jacobsen, R. Sachin, Surve, Perimeter recombination characterization by luminescence imaging, *IEEE Journal of Photovoltaics* 6 (1) (2016) 244–251 <https://doi.org/10.1109/jphotov.2015.2480225>.
- [9] Hannes Höffler, Otwin Breitenstein, Haunschild Jonas, Short-circuit current density imaging via PL image evaluation based on implied voltage distribution, *IEEE Journal of Photovoltaics* 5 (2) (2015) 613–618 <https://doi.org/10.1109/jphotov.2015.2480225>.

- 2014.2379097.
- [10] Fabian Fertig, Milan Padilla, Otwin Breitenstein, Hannes Höffler, Ino Geisemeyer, Martin C. Schubert, Stefan Rein, Short-circuit current density imaging methods for silicon solar cells, *Energy Procedia* 77 (August) (2015) 43–56 <https://doi.org/10.1016/j.egypro.2015.07.008>.
 - [11] David L. Young, Brian Egaas, Pinegar Scott, Stradins Paul, A new real-time quantum efficiency measurement system, 2008 33rd IEEE Photovoltaic Specialists Conference, IEEE, 2008, <https://doi.org/10.1109/pvsc.2008.4922748>.
 - [12] Eric J. Schneller, Kortan Ogutman, Siyu Guo, Winston V. Schoenfeld, Kristopher O. Davis, Crystalline silicon device loss analysis through spatially resolved quantum efficiency measurements, *IEEE Journal of Photovoltaics* 7 (4) (2017) 957–965 <https://doi.org/10.1109/jphotov.2017.2689160>.
 - [13] Mohammad Jobayer Hossain, Bibek Tiwari, Indranil Bhattacharya, Novel high efficiency quadruple junction solar cell with current matching and quantum efficiency simulations, *Sol. Energy* 139 (December) (2016) 100–107 <https://doi.org/10.1016/j.solener.2016.09.031>.
 - [14] Takashi Fuyuki, Hayato Kondo, Tsutomu Yamazaki, Yu Takahashi, Yukihiro Uraoka, Photographic surveying of minority carrier diffusion length in polycrystalline silicon solar cells by electroluminescence, *Appl. Phys. Lett.* 86 (26) (2005) 262108 <https://doi.org/10.1063/1.1978979>.
 - [15] M.K. Juhl, T. Trupke, The impact of voltage independent carriers on implied voltage measurements on silicon devices, *J. Appl. Phys.* 120 (16) (2016) 165702 <https://doi.org/10.1063/1.4965698>.
 - [16] M.D. Abbott, R.A. Bardos, T. Trupke, K.C. Fisher, E. Pink, The effect of diffusion-limited lifetime on implied current voltage curves based on photoluminescence data, *J. Appl. Phys.* 102 (4) (2007) 044502 <https://doi.org/10.1063/1.2756529>.
 - [17] Hannes Höffler, Hasan Al-Mohtaseb, Haunschild Jonas, Bernhard Michl, Kasemann Martin, Voltage calibration of luminescence images of silicon solar cells, *J. Appl. Phys.* 115 (3) (2014) 034508 <https://doi.org/10.1063/1.4862400>.
 - [18] Ziv Hameiri, Pooja Chaturvedi, Keith R. McIntosh, Imaging the local ideality factor by contactless photoluminescence measurement, *Appl. Phys. Lett.* 103 (2) (2013) 023501 <https://doi.org/10.1063/1.4812835>.
 - [19] Chao Shen, Henner Kampwerth, Martin Green, Spatially resolved photoluminescence imaging of essential silicon solar cell parameters, 2012 38th IEEE Photovoltaic Specialists Conference, IEEE, 2012, <https://doi.org/10.1109/pvsc.2012.6317955>.
 - [20] O. Breitenstein, Local analysis of the efficiency of solar cells based on dark lock-in thermography imaging, Proceedings of the 2012 International Conference on Quantitative InfraRed Thermography, QIRT Council, 2012, <https://doi.org/10.21611/qirt.2012.129>.
 - [21] Otwin Breitenstein, Local efficiency analysis of solar cells based on lock-in thermography, *Sol. Energy Mater. Sol. Cell.* 107 (December) (2012) 381–389 <https://doi.org/10.1016/j.solmat.2012.07.019>.
 - [22] Mohammad Jobayer Hossain, Geoffrey Gregory, Hardik Patel, Siyu Guo, Eric Schneller, Andrew Gabor, Zhihao Yang, Adrienne Blum, Kristopher Olan Davis, Detailed performance loss analysis of silicon solar cells using high throughput metrology methods, World Conference on Photovoltaic Energy Conversion (WCPEC-7), 2018.
 - [23] R.A. Sinton, A. Cuevas, A quasi-steady-state open-circuit voltage method for solar cell characterization, Proceedings of the 16th European Photovoltaic Solar Energy Conference, 2000.
 - [24] Stephan Suckow, Tobias M. Pletzer, Kurz Heinrich, Fast and reliable calculation of the two-diode model without simplifications, *Prog. Photovoltaics Res. Appl.* 22 (4) (2012) 494–501 <https://doi.org/10.1002/pip.2301>.
 - [25] Uwe Rau, Superposition and reciprocity in the electroluminescence and photoluminescence of solar cells, *IEEE Journal of Photovoltaics* 2 (2) (2012) 169–172 <https://doi.org/10.1109/jphotov.2011.2179018>.
 - [26] B. Fischer, J. Müller, P.P. Altermatt, A simple emitter model for quantum efficiency curves and extracting the emitter saturation current, 28th European Photovoltaic Solar Energy Conference and Exhibition, 2013.